

Multifunctional Topology Optimization of Strain-Sensing Nanocomposite Beam Structures

Ryan Seifert · Mayuresh Patil · Gary Seidel · Gregory Reich

Received: date / Accepted: date

Abstract Controlling volume fractions of nanoparticles in a matrix can have a substantial influence on composite performance. This paper presents a multi-start topology optimization algorithm that designs nanocomposite structures for objectives pertaining to stiffness and strain sensing. Local effective properties are obtained by controlling local volume fractions of carbon nanotubes (CNTs) in an epoxy matrix, which are assumed to be well dispersed and randomly oriented. Local Young's Modulus, conductivity, and piezoresistive constant drive the global objectives of strain energy and resistance change. Strain energy is obtained via a modified solution of Euler-Bernoulli equations and resistance change is obtained via solution of a bilinear quadrilateral finite element problem. The optimization uses a two-step restart method in which Pareto points from the first step are used as starting conditions in the second step. An efficient method for obtaining analytic sensitivities of the objective functions is presented. The method is used to solve a set of example problems pertaining to the design of a composite beam in bending.

R. Seifert
460 Old Turner St, Blacksburg, VA 24060
Tel.: +302-312-3286
E-mail: rseifert@vt.edu

M. Patil
460 Old Turner St, Blacksburg, VA 24060
Tel.: +540-231-8722
E-mail: mpatil@vt.edu

G. Seidel
460 Old Turner St, Blacksburg, VA 24060
Tel.: +540-231-9897
E-mail: gary.seidel@vt.edu

G. Reich
2210 Eighth St, Wright-Patterson Air Force Base, OH 45433
Tel.: +937-713-7138
E-mail: gregory.reich.1@us.af.mil

The results show that the strain energy may be optimized by placing high volume-fraction CNT elements away from the neutral axis. Resistance change is optimized through a combination of shifting the neutral axis, formation of conductive paths between electrodes, and asymmetric distribution of highly piezoresistive elements. Results also show that the strain energy is governed by the volume fraction constraint and the resistance change is dependent on a combination of the volume fraction constraint and the boundary electrode location.

Keywords Topology Optimization · Multifunctional Optimization · Carbon Nanotubes · Micromechanics · Analytic Sensitivities · Strain Sensing

1 Introduction

Recent developments in advanced materials have led to the emergence of multifunctional structures. "A multifunctional structure combines the functional capabilities of one or more subsystems with that of the load bearing structure" [30]. In addition to reducing the mass and volume of the overall system by integrating subsystems within the structure [28], multifunctional structures may also introduce novel behavior to the system. Within the aerospace field, one of these possible behaviors is self-sensing [11], in which a structure is able to directly collect information about its operating environment and relay that information to pilots, testing engineers, and maintenance engineers. Heavily related to this concept is the idea of the digital twin. The digital model of an aircraft would use systems such as the embedded sensor to track loading conditions of the aircraft throughout its lifetime. Thus, each aircraft would be paired with a digital model detailing the entire flight

history of that craft, allowing maintenance engineers to make more informed decisions about fatigue, damage, etc. [12].

While classical strain measurement systems are relatively inexpensive and are sensitive at the macroscale, they suffer from several drawbacks. They are fixed directional sensors, they have low resolution at nanoscales, and cannot be easily embedded in a structure without disrupting its mechanical behavior [22]. The inability to embed a traditional sensor in the structure is a significant limitation for composites, in which cross-sectional or interlaminar failures may not be observable at the surface [39]. This helps to motivate the investigation of multifunctional structures in which the sensing material is dispersed throughout the structure.

Of the candidate materials for use in creating self-sensing structures, carbon nanotubes (CNTs) are the subject of much attention [22]. CNT based composite strain sensors have been shown to have higher sensitivities than classic strain gauges at the macroscale [10] and exhibit strain sensing through several mechanisms. These include variation of conductive networks formed by CNT contact, tunneling resistance change in neighboring CNTs as distance between neighbors changes, and the inherent piezoresistivity of the CNTs [5].

Over the last several years, additive manufacturing techniques have evolved to allow for the fabrication of complex structures, and have even been extended to nanocomposites. “Additive manufacturing holds strong potential for the formation of a new class of multifunctional nanocomposites through embedding of nanomaterials [15].” In fact, Postiglione et al. have shown it is now possible to additively manufacture CNT/polymer composites with finely tailored microstructures using liquid deposition [25]. This motivates the development of a design algorithm that can combine the developments in multifunctional materials with those of advanced manufacturing processes. For this, topology optimization is a promising candidate.

Recently, much has been done to apply topology optimization to the design of multifunctional materials. Rubio [29] investigated topology optimization of a piezoresistive patch in a compliant mechanism in which orientation of a monolithic Wheatstone bridge was optimized in addition to the topology of the compliant structure. Stanford et. al [37] optimized a carbon fiber reinforced latex wing for an aeroelastic response. These wings were then manufactured and tested, and it was found that even with a low fidelity aeroelastic model the optimization was able to improve upon aerodynamic performance. Sigmund and Torquato [36] used multi-phase topology optimization to design two material structures with extreme thermoelastic coefficients

given constraints on volume fractions of each phase. This behavior came at the cost of a low bulk modulus, reinforcing the need for an optimization routine to design a structure with appropriate bulk stiffness that still maximizes thermoelastic performance. Kruijff [18] optimized a beam-like structure for maximum stiffness and thermal conductivity, and also introduced a micromechanics model to compute the optimal unit cell. This unit cell was then used to determine the macro scale material properties and a Pareto front was created relating thermally conductive optima to maximum stiffness optima. It was found that the material composition of the unit cell lattice structure significantly impacted both thermal and elastic compliance. Maute et. al [19] used level set topology optimization to design a set of printable SMP (shape memory polymer)-elastic matrix composites to match a specified deformed shape once actuated. Zegard and Paulino connected additive manufacturing with topology optimization for a single objective, single material system [42].

However, a majority of published works focus on on/off topologies, in which there are a limited (often 1 or 2) candidate materials. This paper introduces the design of a graded nanocomposite structure, in which any element may contain a different effective material via variation in the local CNT volume fraction. This volume fraction is not penalized or driven to any on/off configuration.

The problem is posed as the design of a strain sensing beam of constant cross-section in order to optimize measures of stiffness and sensing. The beam is loaded with a constant prescribed curvature, representative of a bending test. Constraints are imposed on both the local and global CNT volume fractions as representations of manufacturing and cost constraints, respectively. Micromechanics models are used to obtain element effective properties and are functions of the local CNT volume fraction. The performance of optimal topologies of the cross-sections are compared across different constraint limits and electrostatic boundary conditions, and conclusions are drawn about the usefulness of leveraging topology optimization in the design of distributed multifunctional systems.

Section 2 introduces the general topology optimization algorithm and the specific problem statement. Section 3 follows with the relevant micromechanics, Euler-Bernoulli equations, and formulation of the electrostatic finite element equations. This section also contains the equations necessary for computing the sensitivities of the objective functions with respect to changes in CNT volume fraction. Section 4 introduces the Pareto-Based restart method for finding improved Pareto Fronts in a complex coupled problem with many minima. Re-

sults of this method, as applied to the self-sensing beam for several volume fraction constraints and electrostatic boundary conditions, are shown in Section 5. Conclusions are summarized and possible extensions of the work are highlighted in Section 6.

2 Topology Optimization Overview and Problem Statement

In a single material system, topology optimization seeks to design a structure by first discretizing the design space and then driving the local material volume fractions in each element of that space to their optimal values. The general problem is formulated as follows:

$$\begin{aligned} \min F(\mathbf{v}) &= F(f_1(\mathbf{v}), f_2(\mathbf{v})) \\ \text{s.t. } 0 &\leq v_e \leq 1 \\ &\sum v_e \leq V_p \end{aligned} \quad (1)$$

Here the set of design variables are designated as the vector \mathbf{v} , and may correspond to a ‘relative density’ of material or a phase volume fraction. The relative density in each element is denoted by v_e . The objective function F may be multiobjective, and be formed from single objective functions f_1 and f_2 . For this paper $f_1 = \frac{\Delta R}{R_0}(\mathbf{v})$, the resistance change due to strain, and $f_2 = U(\mathbf{v})$, the strain energy in bending. The design variables are used within one or more material interpolation schemes, which govern the effective material properties of the corresponding element. As an example, consider the classic Solid Isotropic Material with Penalization, or SIMP method [4]. Applying SIMP to an effective Young’s Modulus leads to

$$E_e = v_e^p E_0 \quad (2)$$

where the effective Young’s Modulus at the e th element as a function of the design variables and the material modulus E_0 . The penalty variable, p , is added to drive v_e to either 0 or 1 during the optimization. An element with $v_e = 0$ has no stiffness and an element with $v_e = 1$ has the material stiffness E_0 . There exists some optimal layout of 1’s and 0’s that satisfy the constraint on the total volume fraction permitted, V_p , while minimizing the objective function $F(\mathbf{v})$. For a comprehensive review on topology optimization, see [7] and [4].

Rather than considering a single material property and driving this property to 1 (on) or 0 (off) via the SIMP method, one may instead consider a micromechanics model, such as a rule of mixtures [38,40], inverse rule of mixtures [38,26], or a method that makes use of the Eshelby solution [9], such as the Mori-Tanaka

method [21]. These models relate effective material properties to the volume fraction of an inhomogeneity in a matrix. Therefore, one may substitute a micromechanics model in place of the SIMP method equation above, and the design variables then become the local volume fraction of an inclusion. In the case of this paper, that is the volume fraction of CNT in each element. What results is no longer an ‘on’ or ‘off’ design, but rather a distributed system of CNT-epoxy nanocomposite in which each element may have a different material composition.

In Figure 1 the general optimization algorithm is paired with the steps that pertain to the solution of a topology optimization problem for a multifunctional CNT based composite. The problem of interest, the design of the cross-section of a beam subject to a prescribed curvature, is illustrated in Figure 2. The cross-section is discretized into a 2D finite element mesh and each element is given a single design variable representative of the volume fraction of CNT in that element. There are constraints on both the amount of CNT available to a single element and on the total amount of CNT in the cross-section; v_p and V_p , respectively. For a self-sensing cross-section it is desirable that the structure have some measure of stiffness so that it can perform its structural application. Strain energy was chosen as an objective to capture the stiffness. It is also necessary that a measure of the sensing signal be maximized. Resistance change in the presence of strain is a common measure of a sensor’s capability [23,1], and is selected as the second objective. These objectives will be shown to be competing for a limited amount of CNT, with the stiffness optimization wanting to place material in locations that may be disadvantageous for sensing, and vice-versa. The problem is solved using an epsilon-constraint optimization, in which the strain energy objective is rewritten as a constraint [8,14,20], leading to the optimization problem

$$\begin{aligned} \min F(\mathbf{v}) &= -\frac{\Delta R(\mathbf{v})}{R_0(\mathbf{v})} \\ \text{s.t. } U(\mathbf{v}) &\geq U^* \\ 0 &\leq v_e \leq v_p \\ &\sum v_e \leq V_p \end{aligned} \quad (3)$$

where v_e is the CNT volume fraction of the e th element. $\frac{\Delta R(\mathbf{v})}{R_0(\mathbf{v})}$ is the resistance change between the strained and unstrained cross-section ΔR , normalized by the unstrained resistance, R_0 . U is the strain energy, and U^* is a prescribed strain energy constraint. By changing U^* one can trade relative importance of stiffness versus

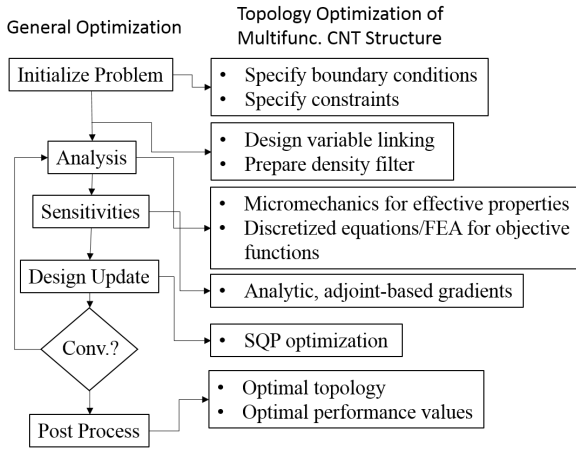


Fig. 1 Topology Optimization Algorithm.

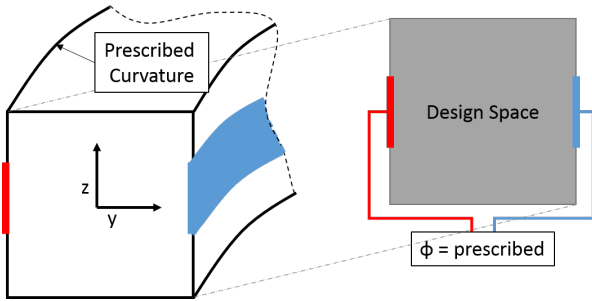


Fig. 2 Beam with prescribed curvature and the cross-section to be designed.

sensing in the design. However, care must be taken in the selection of U^* to ensure the constraint is feasible. Epsilon-constraint method reformulates the multiobjective problem into ‘Give the best value of Objective A while satisfying constraints on Objective B to a threshold’. The remaining two constraints state that there may not be greater than v_p CNT in a given element and the summation of all the CNT volumes must be less than or equal to the global volume fraction constraint, V_p .

3 Analysis and Sensitivity of the Objectives

3.1 Micromechanics

Micromechanics laws relate the design variables to local Young’s Modulus, resistivity, and piezoresistive constant in a given element. It is assumed that within an element the CNT are well dispersed and randomly oriented, giving linear and isotropic effective properties.

3.1.1 Young’s Modulus

At low volume fractions the effective Young’s modulus in a CNT-epoxy composite linearly increases as more

CNT are added [34]. A rule of mixtures model is used to approximate the composite effective Young’s modulus. The rule of mixtures equation is:

$$E_e = E^{CNT} v_e + E^{mat}(1 - v_e) \quad (4)$$

where E_e represents the local effective Young’s Modulus of the e th element, and v_e the local volume fraction of CNT in the e th element. E^{CNT} is the modulus of the CNTs, and E^{mat} is the modulus of the matrix. The rule of mixtures is continuous and differentiable, both desirable qualities when the equation is to be incorporated within an optimization algorithm. By nature of being the highest possible bound on effective modulus, the rule of mixtures model for stiffness acts to add conservatism to the sensing objective, which will be shown to be dependent on strain. The sensitivity of the Young’s modulus with respect to a change in the volume fraction is

$$\frac{dE_e}{dv_e} = E^{CNT} - E^{mat} \quad (5)$$

3.1.2 Resistivity

Small increases in CNT volume fraction can decrease the composite effective resistivity by orders of magnitude [24]. This behavior is seen to be nonlinear even at low volume fractions, requiring use of an inverse rule of mixtures model [27]. Continuing with the assumption that the CNT are randomly oriented and well dispersed, it is assumed that effective resistivity is isotropic and given as

$$\rho_{0e} = \frac{1}{\frac{v_e}{\rho_0^{CNT}} + \frac{1 - v_e}{\rho_0^{mat}}} \quad (6)$$

where ρ_{0e} is the effective resistivity of the e th element with a local CNT volume fraction v_e . The CNT and matrix resistivities are given by ρ_0^{CNT} and ρ_0^{mat} , respectively. The sensitivity is given by

$$\frac{d\rho_{0e}}{dv_e} = -\frac{\frac{1}{\rho_0^{CNT}} - \frac{1}{\rho_0^{mat}}}{(\rho_{0e})^2} \quad (7)$$

3.1.3 Piezoresistive Constant

Piezoresistivity is a property that dictates how changes in strain influence resistivity. A piezoresistive constant, sometimes called a normalized gage factor, can be used to measure this property. The piezoresistive constant is

Table 1 Constants used to form the element effective piezoresistivity

A_1	A_2	A_3	B_1
243613	122516	24571.2	100
B_2	C_1	C_2	C_3
1.05	406.25	16.25	3.9375

denoted as the variable g , and the local effective piezoresistive constant of the e th element is g_e . Bauhofer and Kovacs [3] have shown that depending on the percolation threshold of a given CNT-Epoxy composite, the piezoresistive behavior can exhibit an almost discrete on/off behavior. Below the percolation threshold the piezoresistivity is small, and at the percolation threshold the piezoresistivity is maximized. Alamus et al. and Kuelemans [2,16] show that after crossing percolation, continuing to add CNT will reduce the piezoresistive constant. Depending on the type of nanotube and fabrication procedure, the percolation threshold of CNT-Epoxy composites can be as low as .0025 percent CNT volume fraction [31] but it is most common that this threshold is between 1.5 and 4.5 percent [33,3]. In the current micromechanics model 2 percent volume fraction was chosen for the percolation threshold. The effective piezoresistive constant is small before 2 percent, peaks at the percolation volume fraction of 2 percent, and decreases for larger volume fractions. A curve fit model is used to approximate this behavior.

$$g_e = \begin{cases} \sum_{i=1}^3 A_i \tan((2i-1)\pi v_e) & v_e \leq .015 \\ 2(\cos(B_1\pi v_e) + B_2) & .015 < v_e \leq .02 \\ -C_1 v_e^2 + C_2 v_e + C_3 & .02 < v_e \leq .1 \end{cases} \quad (8)$$

The sensitivity of the piezoresistive constant to the CNT volume fraction is

$$\frac{dg_e}{dv_e} = \begin{cases} \sum_{i=1}^3 A_i (2i-1)\pi \sec^2((2i-1)\pi v_e) & v_e \leq .015 \\ -2B_1\pi \sin(B_1\pi v_e) & .015 < v_e \leq .02 \\ -2C_1 v_e + C_2 & .02 < v_e \leq .1 \end{cases} \quad (9)$$

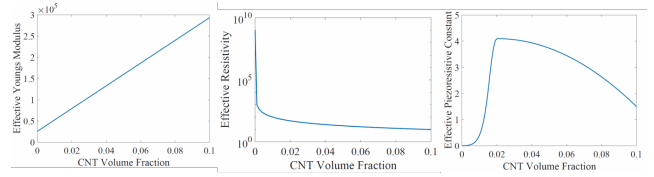
In Equations 8 and 9, the constants A_1 - A_3 , B_1 - B_2 , and C_1 - C_3 are selected to ensure that the curve is continuous and has a continuous first derivative. These parameters may be altered to tune the piezoresistive model to fit a specific manufacturing process and/or available experimental data. Table 1 shows the values identified for these constants in this paper.

Table 2 Matrix and fiber material properties

	CNT	Epon
Resistivity ρ_0 (ohm/cm)	1	1e9
Young's Modulus E (GPA)	270	2.6

3.1.4 Material Properties and Micromechanics Plots

Material properties for CNT and Epon 862 are presented in Table 2 [33,43]. It should be noted that the Poisson's ratio of the nanocomposite was assumed to be a constant $\nu = 0.3$. Effective Poisson's ratios of CNT-Epon composites were modeled using a Mori-Tanaka method in [6,13], where it was found that for aligned CNT the composite effective properties were $\nu_{12}^{eff} = 0.3772$, $\nu_{23}^{eff} = \nu_{13}^{eff} = .2629$. For randomly oriented nanotubes it can be assumed that these values may be averaged, resulting in an effective Poisson's ratio of .300. The micromechanics equations are plotted against CNT volume fraction in Figure 3.

**Fig. 3** Local effective properties as a function of CNT volume fraction.

3.2 Strain Energy of a Beam with Prescribed Curvature

The strain energy of a beam in bending can be related directly to bending rigidities and the bending curvatures. Bending rigidities may be computed from modified Euler-Bernoulli beam equations [17] as

$$\begin{aligned} EI_z &= \int E y^2 dA = \sum_{e=1}^{nele} E_e y_e^2 A_e \\ EI_y &= \int E z^2 dA = \sum_{e=1}^{nele} E_e z_e^2 A_e \\ EI_{yz} &= \int E y z dA = \sum_{e=1}^{nele} E_e y_e z_e A_e \end{aligned} \quad (10)$$

where y_e and z_e are distances from the cross-section centroid of a beam with the x direction oriented along the beam's length. These are given by

$$\begin{aligned} z_e &= Z_e - Z_c \\ y_e &= Y_e - Y_c \end{aligned} \quad (11)$$

where Y_e and Z_e are locations of the element centers in the cross-section. Z_c and Y_c coordinates of the neutral axis, given by

$$\begin{aligned} Z_c &= \frac{\sum_{e=1}^{nele} E_e Z_e A_e}{\sum_{e=1}^{nele} E_e^{eff} A_e} \\ Y_c &= \frac{\sum_{e=1}^{nele} E_e Y_e A_e}{\sum_{e=1}^{nele} E_e^{eff} A_e} \end{aligned} \quad (12)$$

The bending rigidities may then be related to bending moment as

$$\begin{bmatrix} M_y \\ M_z \end{bmatrix} = \begin{bmatrix} EI_y & EI_{zy} \\ EI_{zy} & EI_z \end{bmatrix} \begin{bmatrix} \kappa_y \\ \kappa_z \end{bmatrix} \quad (13)$$

where κ_y and κ_z are the bending curvatures about the y and z axes. Here the problem may be simplified if the bending is applied about a single axis, and symmetry is enforced. For example let $\kappa_y = 0$, and symmetry dictates that $EI_{zy} = 0$. The only remaining component of the moment is $M_z = EI_z \kappa_z$.

The strain energy is then given by

$$U = \frac{1}{2} \frac{M_z^2}{EI_z} = \frac{1}{2} EI_z \kappa_z^2 \quad (14)$$

and the sensitivity of the strain energy with respect to a change in the design variables is computed as

$$\frac{\partial U}{\partial v_e} = \frac{1}{2} \frac{\partial EI_z}{\partial v_e} \kappa_z^2 \quad (15)$$

Equation 14 shows that for a prescribed curvature, maximization of the strain energy corresponds to a maximization of the bending rigidity. Sensitivity of the strain energy is then dependent on the sensitivity of the bending rigidity with respect to the element volume fractions, which is given by

$$\frac{\partial EI_z}{\partial v_e} = \frac{dE_e}{dv_e} y_e^2 A_e + 2 \sum_{e=1}^{nele} E_e y_e \frac{\partial y_e}{\partial v_e} A_e \quad (16)$$

where $\frac{dE_e}{dv_e}$ comes from the micromechanics equations. The sensitivity of the change in the Y_c with respect to the change in design variable must also be considered.

$$\frac{\partial y_e}{\partial v_e} = \frac{\frac{dE_e}{dv_e} A_e \left(\sum_{e=1}^{nele} E_e Y_e A_e \right) - \frac{dE_e}{dv_e} Y_e A_e \left(\sum_{e=1}^{nele} E_e A_e \right)}{\left(\sum_{e=1}^{nele} E_e A_e \right)^2} \quad (17)$$

3.3 Resistance Change

In classic strain sensors the gage factor is used to convert the measured resistance of a sensor into an approximation of strain. Gage factor is defined as the change in resistance between the strain and unstrained cross section divided by the unstrained resistance and the strain. Maximizing the resistance change between the strained and unstrained structure leads to an increase in signal-to-noise ratio in strain sensing.

The resistance change maximization problem is formulated based on Figure 2. A set of electrodes, denoted by the red and blue bars, are located on the boundary of the cross-section and are used to prescribe a voltage difference. The cross-section is also subject to the same curvature as the strain energy maximization problem, and thus the same strain field. Two solutions of an electrostatics finite element problem are required to obtain the resistance change. The finite element solution is used to obtain the unstrained and the strained currents, which may be related to the resistance through Ohm's law.

3.3.1 Electric Current

The electrostatics continuity equation (conservation of charge) states that the divergence of the current density (Ψ) is 0.

$$\nabla \cdot \Psi = 0 \quad (18)$$

Current density is related to electric conductivity (σ) and the electric field (E) via Ohm's law as

$$\Psi = \sigma E \quad (19)$$

The electric field is the negative of the gradient of the potential. Substituting this into Equation 18 gives

$$\nabla \cdot \Psi = -\nabla \cdot (\sigma \nabla \phi) = 0 \quad (20)$$

In the 2D case the electric potential varies in the z and the y directions, $\phi = \phi(z, y)$. Conductivity may also change in both directions, $\sigma = \sigma(z, y)$. Rewriting the equation gives

$$\frac{\partial}{\partial z} \left(\sigma(z, y) \frac{\partial \phi(z, y)}{\partial z} \right) + \frac{\partial}{\partial y} \left(\sigma(z, y) \frac{\partial \phi(z, y)}{\partial y} \right) = 0 \quad (21)$$

The governing equations are discretized via the finite element method, resulting in the algebraic equations

$$\mathbf{C}\phi = \mathbf{f} \quad (22)$$

or, for a given element

$$\mathbf{C}_e\phi_e = \mathbf{f}_e \quad (23)$$

where \mathbf{C}_e is the element electrostatic ‘stiffness’ matrix, ϕ_e is the element electric potential vector, and \mathbf{f}_e is the element current vector. The electrostatic version of the stiffness matrix depends on the conductivity matrix σ .

$$\mathbf{C}_e(v_e) = \int_{\xi} \int_{\eta} \mathbf{B}^T \sigma_e \mathbf{B} |\mathbf{J}_e| d\xi d\eta \quad (24)$$

where \mathbf{B} is the gradient matrix, $|\mathbf{J}_e|$ is the determinant of the element Jacobian, and $\sigma_e = \begin{bmatrix} \sigma_{z_e} & 0 \\ 0 & \sigma_{y_e} \end{bmatrix}$ and is determined by the local element volume fraction. Prior to the application of strain, i.e. non-piezoresistive problem, the current is calculated from element conductivities of the form $\sigma_z = \sigma_y = \frac{1}{\rho_{0_e}}$. For the coupled problem with strain applied, the piezoresistive term will be added and discussed in a later section.

Equation 22 is divided into submatrices based on which degrees of freedom are constrained. The subscript u denotes degrees of freedom which are unspecified, but on the boundary. The subscript s indicates these degrees of freedom are part of the boundary condition, and have their electric potential specified. This represents specifying the placement of electrodes on the structure. Finally, the subscript i indicated degrees of freedom on the interior of the cross-section.

$$\begin{bmatrix} \mathbf{C}_{ii} & \mathbf{C}_{iu} & \mathbf{C}_{is} \\ \mathbf{C}_{iu} & \mathbf{C}_{uu} & \mathbf{C}_{us} \\ \mathbf{C}_{is} & \mathbf{C}_{us} & \mathbf{C}_{ss} \end{bmatrix} \begin{bmatrix} \phi_i \\ \phi_u \\ \phi_s \end{bmatrix} = \begin{bmatrix} \mathbf{f}_i \\ \mathbf{f}_u \\ \mathbf{f}_s \end{bmatrix} \quad (25)$$

In this equation the entire \mathbf{C} matrix is known, and $\phi_s = \phi_{s0}$ is known along the electrodes. $\mathbf{f}_u = \mathbf{f}_i = 0$ unless non-electrode boundary or interior currents are specified. There are two forms of these equations that are convenient for use in solving and obtaining sensitivities.

Form A:

$$\begin{bmatrix} \mathbf{C}_{ii} & \mathbf{C}_{iu} & 0 \\ \mathbf{C}_{iu} & \mathbf{C}_{uu} & 0 \\ 0 & 0 & \mathbf{II} \end{bmatrix} \begin{bmatrix} \phi_i \\ \phi_u \\ \phi_s \end{bmatrix} = \begin{bmatrix} -\mathbf{C}_{is}\phi_{s0} \\ -\mathbf{C}_{us}\phi_{s0} \\ \phi_{s0} \end{bmatrix} \quad (26)$$

or, in simplified Form A: $\hat{\mathbf{C}}\phi = \mathbf{b}$. Here the symbol \mathbf{II} is used to represent the identity matrix.

Total current, I_{bc} , is measured as the summation of the nodal currents across a boundary electrode. The vector q is created to aid in the summation. q has a value of 1 for degrees of freedom on the boundary electrode to be summed over, and is 0 for the degrees of freedom on the other boundary electrode.

$$I_{bc} = \mathbf{q}^T [\mathbf{C}_{is}^T \mathbf{C}_{us}^T \mathbf{C}_{ss}^T] \phi = \mathbf{p}^T \phi \quad (27)$$

The adjoint method is used to obtain the sensitivity of the current. The total derivative is

$$\frac{dI_{bc}}{dv_e} = \frac{\partial I_{bc}}{\partial v_e} + \frac{\partial I_{bc}}{\partial \phi} \frac{\partial \phi}{\partial v_e} \quad (28)$$

The state equation is used to help solve the above equation. The state equation is $\hat{\mathbf{C}}\phi - \mathbf{b} = \mathbf{0}$. As this equation is equal to 0, the derivative is also 0 and is given as

$$\frac{\partial \hat{\mathbf{C}}}{\partial v_e} \phi + \hat{\mathbf{C}} \frac{\partial \phi}{\partial v_e} - \frac{\partial \mathbf{b}}{\partial v_e} = \mathbf{0} \quad (29)$$

The sensitivity equation is appended with the above equation times the adjoint variable, λ . Rearranging leads to

$$\frac{dI_{bc}}{dv_e} = \frac{\partial I_{bc}}{\partial v_e} + \lambda^T \left(\frac{d\mathbf{b}}{dv_e} - \frac{d\hat{\mathbf{C}}}{dv_e} \phi \right) + \left(\frac{\partial I_{bc}}{\partial \phi} - \lambda^T \hat{\mathbf{C}} \right) \frac{\partial \phi}{\partial v_e} \quad (30)$$

where λ may be chosen as any arbitrary vector. It is convenient to select a λ that makes the third term in the above equation 0. This results in the adjoint state equation:

$$\hat{\mathbf{C}}\lambda = \left(\frac{\partial I_{bc}}{\partial \phi} \right)^T = \mathbf{p} \quad (31)$$

which is solved for λ and substituted to obtain the adjoint form of the sensitivity.

$$\frac{dI_{bc}}{dv_e} = \frac{\partial I_{bc}}{\partial v_e} + \lambda^T \left(\frac{d\mathbf{b}}{dv_e} - \frac{d\hat{\mathbf{C}}}{dv_e} \phi \right) \quad (32)$$

It is now necessary to derive each of the terms: $\frac{\partial I_{bc}}{\partial v_e}$,

$$\frac{d\mathbf{b}}{dv_e}, \text{ and } \frac{d\hat{\mathbf{C}}}{dv_e}.$$

$$\frac{\partial I_{bc}}{\partial v_e} = \mathbf{q}^T \left(\frac{d}{dv_e} [\mathbf{C}_{is}^T \mathbf{C}_{us}^T \mathbf{C}_{ss}^T] \right) \phi \quad (33)$$

$$\frac{d\mathbf{b}}{dv_e} = \left(\frac{d}{dv_e} \begin{bmatrix} -\mathbf{C}_{is} \\ -\mathbf{C}_{us} \\ \mathbf{II} \end{bmatrix} \right) \phi_{s0} \quad (34)$$

$$\frac{d\hat{\mathbf{C}}}{dv_e} = \frac{d}{dv_e} \begin{bmatrix} \mathbf{C}_{ii} & \mathbf{C}_{iu} & 0 \\ \mathbf{C}_{iu}^T & \mathbf{C}_{uu} & 0 \\ 0 & 0 & \mathbf{II} \end{bmatrix} \quad (35)$$

The above equations depend on the sensitivities of the electrostatic stiffness matrix with respect to changes in the design variables. As these variables (the CNT volume fractions in each element) are local, sensitivity of a particular element matrix can be used for the sensitivity of the element volume fraction.

$$\frac{\partial \mathbf{C}_e}{\partial v_e} = \mathbf{B}^T \frac{\partial \boldsymbol{\sigma}_e}{\partial v_e} \mathbf{B} | \mathbf{J} |_e \quad (36)$$

$$\frac{\partial \boldsymbol{\sigma}_e}{\partial v_e} = \begin{bmatrix} \frac{\partial \sigma_{z_e}}{\partial v_e} & 0 \\ 0 & \frac{\partial \sigma_{y_e}}{\partial v_e} \end{bmatrix} \quad (37)$$

where $\frac{\partial \sigma_{z_e}}{\partial v_e}$ and $\frac{\partial \sigma_{y_e}}{\partial v_e}$ have explicit known values based on the micromechanics laws used. All the terms needed to solve for the sensitivity are now known.

Care must be taken to choose the correct indices for each v_e , as each v_e corresponds to an element, and that element may have nodal degrees of freedom that lie on the interior, on the unprescribed boundary, and/or on the electrode. This can be simplified if the adjoint method is applied to the alternate solution of the current.

Form B:

$$\begin{bmatrix} \mathbf{C}_{ii} & \mathbf{C}_{iu} & 0 \\ \mathbf{C}_{iu}^T & \mathbf{C}_{uu} & 0 \\ \mathbf{C}_{is}^T & \mathbf{C}_{us}^T & -\mathbf{II} \end{bmatrix} \begin{bmatrix} \phi_i \\ \phi_u \\ \mathbf{f}_s \end{bmatrix} = \begin{bmatrix} -\mathbf{C}_{is} \phi_{s0} \\ -\mathbf{C}_{us} \phi_{s0} \\ -\mathbf{C}_{ss} \phi_{s0} \end{bmatrix} \quad (38)$$

And the simplified Form B: $\tilde{\mathbf{C}} \mathbf{y} = \tilde{\mathbf{b}}$. The solution follows the same steps as the solution of Form A. First, the current is given as

$$I_{bc} = [\mathbf{0} \ \mathbf{0} \ \mathbf{q}]^T \mathbf{y} \quad (39)$$

Then the adjoint equation (the state variable is now \mathbf{y} instead of ϕ) is updated

$$\tilde{\mathbf{C}}^T \tilde{\boldsymbol{\lambda}} = \frac{\partial I_{bc}}{\partial \mathbf{y}} = \mathbf{q}^T \quad (40)$$

and finally the sensitivity equation is updated as

$$\frac{dI_{bc}}{dv_e} = \frac{\partial I_{bc}}{\partial v_e} + \tilde{\boldsymbol{\lambda}}^T \left(\frac{d\tilde{\mathbf{b}}}{dv_e} - \frac{d\tilde{\mathbf{C}}}{dv_e} \mathbf{y} \right) \quad (41)$$

Here the form of I_{bc} is convenient in that $\frac{\partial I_{bc}}{\partial v_e} = 0$.

Furthermore, it is noted that $(\frac{d\tilde{\mathbf{b}}}{dv_e} - \frac{d\tilde{\mathbf{C}}}{dv_e} \mathbf{y})$ may be rearranged, as it is a derivative of the original electrostatic equations, $\mathbf{C} \boldsymbol{\phi} = \mathbf{f}$

$$\frac{d}{dv_e} \begin{bmatrix} -\mathbf{C}_{is} \phi_{s0} \\ -\mathbf{C}_{us} \phi_{s0} \\ -\mathbf{C}_{ss} \phi_{s0} \end{bmatrix} - \frac{d}{dv_e} \left(\begin{bmatrix} \mathbf{C}_{ii} & \mathbf{C}_{iu} & 0 \\ \mathbf{C}_{iu}^T & \mathbf{C}_{uu} & 0 \\ \mathbf{C}_{is}^T & \mathbf{C}_{us}^T & -\mathbf{II} \end{bmatrix} \right) \begin{bmatrix} \phi_i \\ \phi_u \\ \mathbf{f}_s \end{bmatrix} = -\frac{d\mathbf{C}}{dv_e} \boldsymbol{\phi} \quad (42)$$

The differentiation of the Form B equations is independent of whether or not the element contains boundary degrees of freedom.

$$\frac{dI_{bc}}{dv_e} = -\tilde{\boldsymbol{\lambda}}^T \frac{d\mathbf{C}}{dv_e} \boldsymbol{\phi} = -\tilde{\boldsymbol{\lambda}}_e^T ((\mathbf{B}^T \frac{\partial \boldsymbol{\sigma}_e}{\partial v_e} \mathbf{B} | \mathbf{J} |_e) \phi_e) \quad (43)$$

3.3.2 Resistance Change due to Strain

Resistance change due to strain, $\frac{\Delta R}{R_0}$, is measured as the difference in resistance between the unstrained structure (R_0) and the resistance of the strained structure (R_ϵ), normalized by the unstrained resistance i.e.

$$\frac{\Delta R}{R_0} = \frac{R_\epsilon - R_0}{R_0} \quad (44)$$

Resistance is related to current through Ohm's law, $R = \frac{V}{I} = \frac{\Delta \phi}{I_{bc}}$. $\Delta \phi$ is the prescribed potential difference across the electrodes, and is a constant for both the strained and unstrained resistances. This allows for simplification of the resistance change function.

$$\frac{\Delta R}{R_0} = \frac{R_\epsilon - R_0}{R_0} = \frac{I_{bc0}}{I_{bc\epsilon}} - 1 \quad (45)$$

Thus, the resistance change requires the calculation of two different currents. The currents may be calculated using the equations in the previous section, but differ in the formulation of the conductivity matrix. The unstrained element conductivity matrix is

$$\boldsymbol{\sigma}_{0e} = \begin{bmatrix} \frac{1}{\rho_{0e}} & 0 \\ \rho_{0e} & \frac{1}{\rho_{0e}} \end{bmatrix} \quad (46)$$

where ρ_{0e} is given explicitly by Equation 6, and has a sensitivity given by Equation 7. The sensitivity of the unstrained conductivity matrix is then

$$\frac{\partial \sigma_{0_e}}{\partial v_e} = \begin{bmatrix} -\frac{\partial \rho_{0_e}}{\partial v_e} & 0 \\ \rho_{0_e}^2 & -\frac{\partial \rho_{0_e}}{\partial v_e} \\ 0 & \rho_{0_e}^2 \end{bmatrix} \quad (47)$$

Once the structure is loaded the resistivity changes due to the piezoresistive effect. This adds an additional term to the resistivity equation [41, 5]. For a beam with prescribed bending curvature about a single axis it is assumed that the axial strain dominates this response. The resistivity of the e^{th} element in the presence of strain is given as

$$\rho_{\epsilon_e} = \rho_{0_e}(1 + g_e \epsilon_{xx_e}) \quad (48)$$

The above equation leads to changes in the sensitivity as the piezoresistive constant is a direct function of the element volume fraction. Also, the axial strain in an element depends on the prescribed curvature and the distance of the element from the centroid.

$$\epsilon_{xx_e} = \kappa_z y_e \quad (49)$$

Thus, the sensitivity of the strained resistivity is

$$\frac{\partial \rho_{\epsilon_e}}{\partial v_e} = \frac{\partial \rho_{0_e}}{\partial v_e}(1 + g_e \kappa_z y_e) + \rho_{0_e} \frac{\partial g_e}{\partial v_e} \kappa_z y_e + \rho_{0_e} g_e \kappa_z \frac{\partial y_e}{\partial v_e} \quad (50)$$

where $\frac{\partial \rho_{0_e}}{\partial v_e}$ is given by Equation 7, $\frac{\partial g_e}{\partial v_e}$ is given by Equation 9, and $\frac{\partial y_e}{\partial v_e}$ is given by Equation 17. Finally, Equations 48 and 50 are substituted into Equations 46 and 47, which are in turn used to solve for strained current and sensitivity by repeating either the Form A or Form B calculations from the previous section.

4 A Pareto-Based Restart Method for Problems with Multiple Minima

Multifunctional topology optimization is known to exhibit flat design spaces and local minima [32]. The presence of local minima means that the starting condition may have a significant influence on the resulting topology and performance. It is beneficial to develop a multi-start method that can efficiently cover a large amount of the design space without sacrificing final performance.

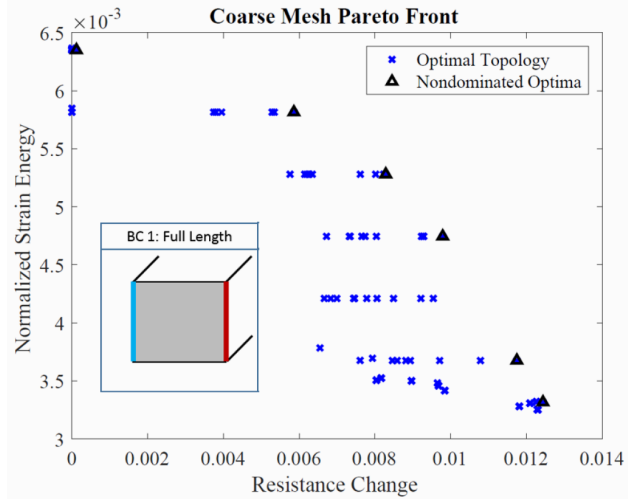


Fig. 4 Results of the coarse mesh optimization with a 2 percent volume fraction constraint and the electrode boundary condition shown in the insert.

While topology optimization exhibits mesh dependence [35], coarse mesh optima may capture general trends in the solution that can be scaled to a finer mesh. The restart method implemented here takes advantage of this fact. It first uses a multi-start method on a coarse mesh to solve a simplified version of the problem. Coarse mesh solutions are computationally inexpensive, and many starting conditions can be used to get better coverage of the design space. The best (Pareto optimal) results of the coarse mesh optimization are then selected, scaled up to a finer mesh size, and used to restart the problem. Thus, a comparatively small amount of starting conditions are used for the more expensive, fine mesh phase.

Consider the cross-section optimization of a beam in bending, subject to a two percent global volume fraction constraint, a ten percent local volume fraction constraint, and with prescribed electrodes shown in the diagram inserted into Figure 4. The design problem is

$$\begin{aligned} \min F(\mathbf{v}) &= -\frac{\Delta R(\mathbf{v})}{R_0(\mathbf{v})} \\ \text{s.t. } U(\mathbf{v}) &\geq U^* \\ 0 &\leq v_e \leq .1 \\ \sum v_e &\leq .02 \end{aligned} \quad (51)$$

Figure 4 also shows the results of a coarse mesh multiobjective optimization in which high resistance change and high strain energy are preferred. All results in this paper were obtained by using Sequential Quadratic Programming (SQP) within Matlab's *fmincon* optimization package. Function decrease tolerance,

constraint feasibility tolerance, and optimality tolerance were all set to $1E - 6$. Each point on the figure is the result of one full optimization of the coarse mesh problem, and was obtained by optimizing with a coarse mesh random initial condition. The tiers in the strain energy constraint were obtained by first performing single objective optimization to obtain approximate utopia points. These points were used to set the bounds on the epsilon-constraint, which was linearly varied between these bounds. Additionally, one set of the random initial conditions was performed with an inactive strain energy constraint, hence the lack of tiered structuring in the bottom right of the figure.

The best points from this set of solutions are marked as nondominated points by the black triangles. The topologies which correspond to these points are scaled to the finer restart mesh size, and are used to start the finer scale, computationally expensive optimization. In the presented example, the fine mesh contains 1600 elements and the coarse mesh contains 400 elements. This four-to-one increase affects both the number of design variables in the optimization problem and also the number of elements and associated degrees of freedom in the analysis and sensitivities of the objectives, resulting in a much larger design problem. The relative errors in strain are less than $1e-10$ percent when comparing the same topology in coarse or fine mesh. The relative errors in the strained resistance are on the order of three to four percent when going from 400 elements to 1600 elements. As the method re-optimizes at the fine mesh and furthermore uses multiple coarse Pareto optimal starting points, it is able to handle discretization errors of these sizes when moving from coarse to fine meshes.

Applying the Pareto-based restart to Figure 4 results in Figure 5, where the triangles mark the starting conditions kept from the coarse mesh phase, the blue circles mark refined mesh optima, and the red circles mark the new Pareto Front. In this example problem the restart with a finer mesh is able to improve upon the initial topologies provided by the coarse mesh optimization.

It is important to note that every nondominated point from the coarse mesh is used as a starting point for every epsilon-constraint level in the refined mesh optimization. The importance of this is illustrated in Figure 6. Here the set of coarse mesh nondominated points, marked by the triangles, are color coded. The circles represent results of a refined mesh restart optimizations, and the color of the circle indicates which coarse mesh topology was used to restart that particular case. It is seen that certain coarse optima may be better restart points than others, even if they are far from the original location in the objective space. For

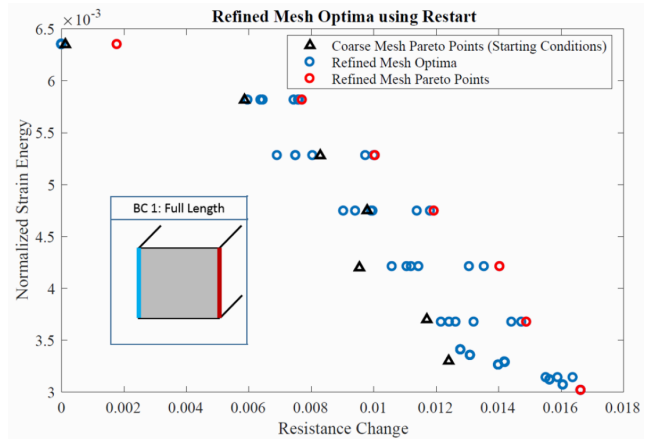


Fig. 5 Restart Method results for a 2 percent volume fraction constraint and the electrode boundary condition shown in the insert.

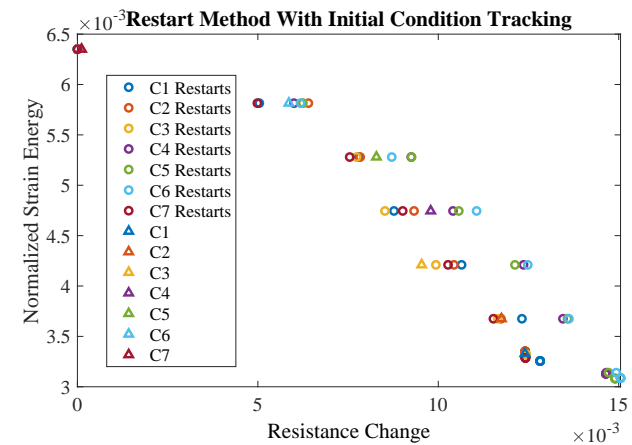


Fig. 6 Restart Method with starting condition tracking. Coarse mesh optima are used as starting conditions.

example, restarting with the topology corresponding to the cyan triangle, C6 Nondom, returns nondominated points for the restart method at 4 locations, all of which are located on a different strain energy tier than the C6 Nondom point itself.

As seen in Figure 7, the restart method provides better optima than just using random starting conditions at refined mesh scale. The restart method was also more computationally efficient, arriving at better optima in 37.2 percent of the CPU time required to obtain the refined mesh results using just a random start.

5 Results

The problem illustrated in Section 4 is reintroduced here, and eight test cases are formed. In each case the restart method is used to solve the multiobjective topology optimization for a beam with prescribed electrode

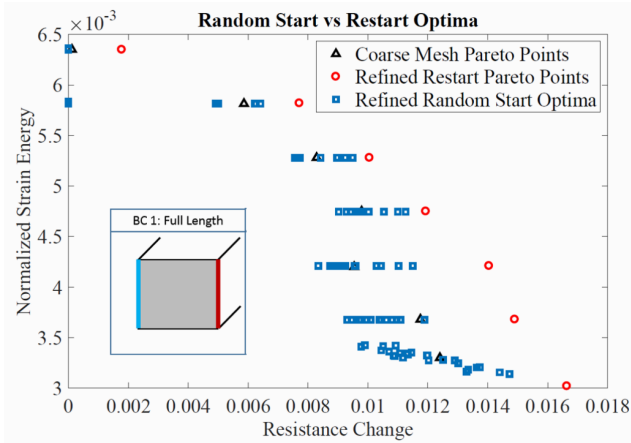


Fig. 7 Comparing random start vs restart optima for 2 percent volume fraction constraint and the electrode boundary condition shown in the insert.

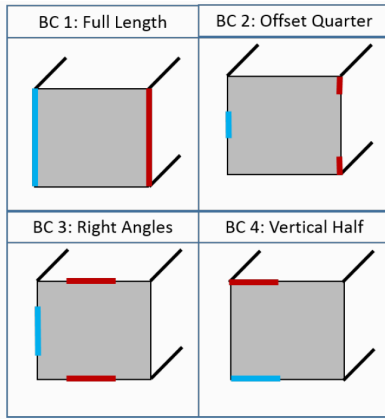


Fig. 8 Boundary condition electrode placement.

configuration. Four electrode boundary conditions are considered along with two volume fraction constraints. The boundary conditions are labeled and illustrated in Figure 8. For each boundary condition a test case is formulated with a two percent global volume fraction constraint and without any global volume fraction constraint. This results in a total of eight applications of the restart method to generate eight Pareto Fronts.

The problem is solved first for a two percent global volume fraction constraint, as was first shown in Section 4 for a single boundary condition. It is now solved for the all four boundary conditions. The process is then repeated with the global volume fraction constraint removed. For each Pareto Front a coarse mesh of 20×20 elements is first optimized. The coarse mesh uses eleven different epsilon-constraint values and ten different random starting conditions, for 110 total coarse optimizations. The nondominated points from this mesh have their associated topologies scaled to a 40×40 mesh and used as initial conditions for the restart method.

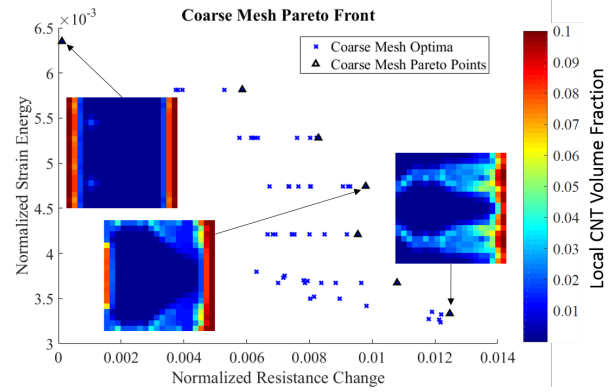


Fig. 9 Coarse mesh multi-start results for a 2 percent volume fraction constraint and BC1.

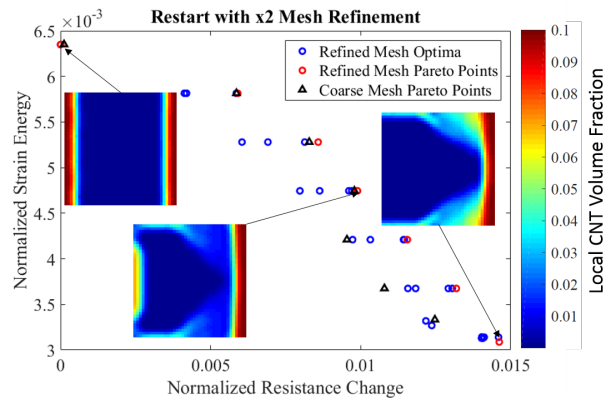


Fig. 10 Refined mesh restart method results for a 2 percent volume fraction constraint and BC1.

Figure 9 presents the coarse mesh multi-start optimization results for a two percent global volume fraction constraint and the full length electrode boundary condition, BC1. This is the same set of optima as Figure 4, now with three of the optimal topologies overlaid to indicate where they fall in the design space. The color bar represents local CNT volume fraction in each element. The restart method results for this problem are shown in Figure 10, showing increased detail in the design and the associated increase in performance. This process is repeated across the array of constraints and boundary conditions in the following sections.

5.1 Strain Energy and Resistance Change Optimization with a Two Percent Global Volume Fraction Constraint

The refined mesh Pareto Fronts associated with the two percent global volume fraction constraint are shown in Figure 11. A Pareto Front is shown for each of the 4 boundary conditions illustrated in Figure 8. Numbered markers are used to relate the specific point to its topology in Figure 12. The numbering convention is laid

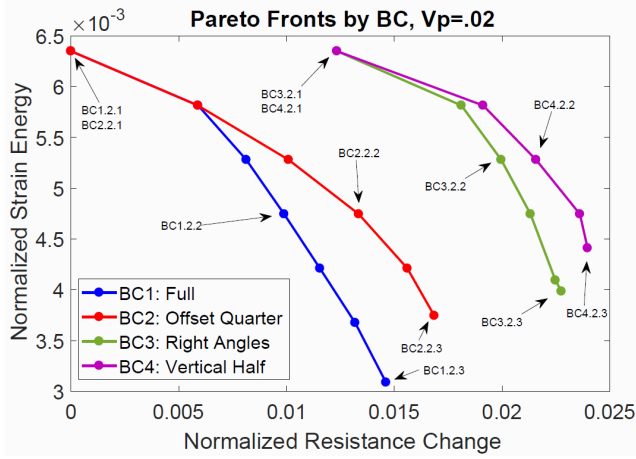


Fig. 11 Pareto Fronts with labeled nondominated points. 2% global VF constraint.

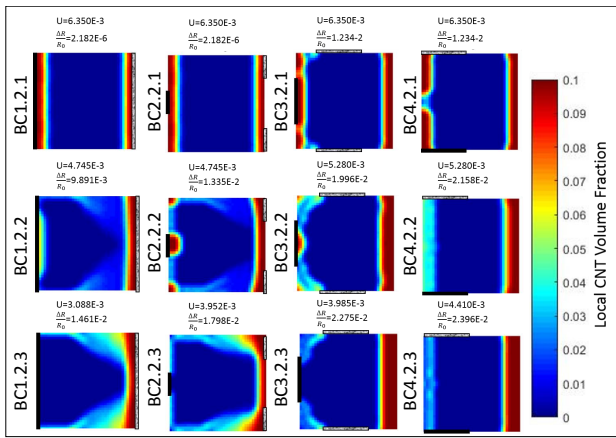


Fig. 12 Comparing topologies with a 2 percent volume fraction constraint. Black and grey bars are used to mark electrode locations on the cross-sections. Labels associate the topology with its associated Pareto point in Figure 11.

out as Electrode Configuration. Volume Fraction Constraint. Topology Index. Thus, label BC1.2.1 is used to mark a design that was optimized with the BC1 electrode configuration, a two percent volume fraction constraint, and is indexed as topology number 1, indicating a high strain energy constraint. Each labeled topology is presented with its strain energy and resistance change. Boxed black and grey lines on the boundary of the topologies mark the electrode locations and the color bar maps the local CNT volume fraction.

BC1.2.1-BC4.2.1 are all topologies that maximize stiffness. Stiffness is maximized by placing high concentrations of CNT away from the bending axis. This sandwich beam configuration is somewhat intuitive, as bending rigidity is effectively an integration of local element stiffness multiplied by the distance from the bending axis.

BC1.2.3-BC4.2.3, are all topologies that maximize the resistance change objective for the given electrode boundary condition. All share a stiff right side and a conductive path of lower volume fraction elements connecting the electrodes. Note that higher volume fraction elements cause horizontal shifts in the neutral axis location, leading to higher strains on the opposite side of the cross-section. As piezoresistivity is dependent on the strain it is beneficial to put highly piezoresistive material in the region opposite the highly stiff elements. Also, the micromechanics equation for resistivity in the presence of strain, Equation 48, is sign dependent. Two elements of the same volume fraction on opposite sides of the neutral axis may generate canceling resistance change contributions. This further reinforces the asymmetric behavior seen in these topologies. The stiff material pulls the neutral axis in that direction and the highly piezoresistive material on the opposite side take advantage of the larger strains.

In all cases, a conductive path between the electrodes is necessary to measure resistance. For BC1 and BC2 this path must cross the neutral axis. For these electrode configurations there will always be some piezoresistive elements on both sides of the neutral axis in the path, resulting in some canceling of piezoresistivity. Additionally, the formation of the conductive path across the neutral axis forces material towards the center of the cross section, which is sub-optimal for stiffness maximization.

The competing relationship between stiffness and resistance change can be partially decoupled by placing the electrodes on one side of the neutral axis, as per BC3 and BC4. For these electrode configurations the highly piezoresistive elements form a conductive path located on one side of the strain field. Adding the stiff elements on the opposite side, the right edge in the topologies shown, moves the neutral axis in that direction without it reducing the total piezoresistive contributions. This also improves strain energy performance by allowing the design to form a conductive path while maintaining a sandwich beam topology.

Figure 13 helps to further illustrate this behavior by plotting the local resistivity change due to strain along with a vector plot to show the conductive path. The red and green colormap shows positive and negative piezoresistive contributions, respectively. Elements within the conductive path will contribute to the resistance change objective. The left and right plots correspond to BC1.2.3 and BC4.2.3, respectively. While there is a band of red elements in right topology shown in the figure, these elements do not fall in the conductive path and do not detract from the sensing performance. Conversely, in the left topology the conductive

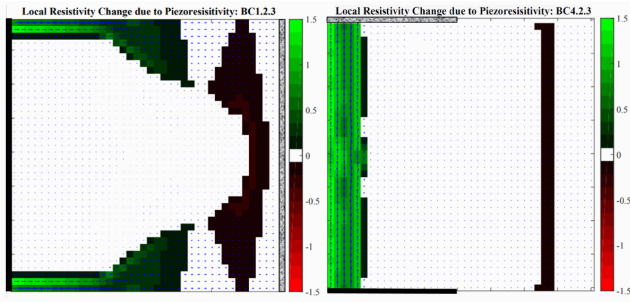


Fig. 13 Comparing local piezoresistive contributions for BC1.2.3 and BC4.2.3. Colormap shows signed change in local resistivity due to strain. Vector plot shows the conductive path.

path flows from left to right, and there will be some subtractive contribution from the red elements.

The influence of boundary condition is evident when comparing points BC1.2.1 and BC2.2.1 to BC3.2.1 and BC4.2.1, in which all designs are able to obtain the same strain energy value. BC1 and BC2 must sacrifice the formation of a conductive path between their left and right electrodes and any asymmetry along this path to obtain the strain energy value required by the epsilon-constraint. BC3 and BC4 form a conductive path to their top and bottom electrodes while still moving stiff material away from the neutral axis. These electrode configurations are able to produce equivalent strain energy values with higher resistance change values.

5.2 Strain Energy and Resistance Change Optimization without a Global Volume Fraction Constraint

The unconstrained results are shown in Figures 14 and 15. Here the label 'UC' in the topology labels refers to designs that are unconstrained in the global volume fraction. Removing the volume fraction constraint provides a 90% increase in the normalized strain energy, when compared to the two percent constrained solution. As adding CNTs always increases the stiffness, there is a direct relationship between the global volume fraction constraint and the strain energy of the cross-section.

As the strain energy constraint is relaxed and the resistance change increases, the design does not use all the available material. BC4.UC.3, the topology with the greatest resistance change of all the presented results, uses less than four percent CNT globally. The same mechanisms for improving sensing are repeated here. A stiff right hand side is used to shift the neutral axis, netting larger strains on the left half of the topology. A conductive path connects the electrodes, and piezore-

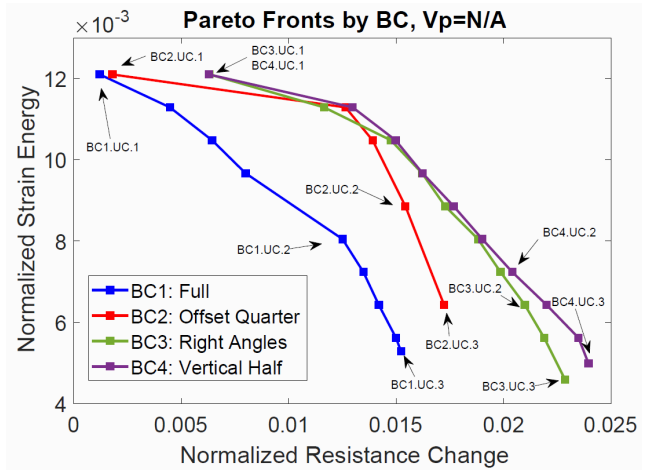


Fig. 14 Pareto Fronts with labeled nondominated points. No global VF constraint.

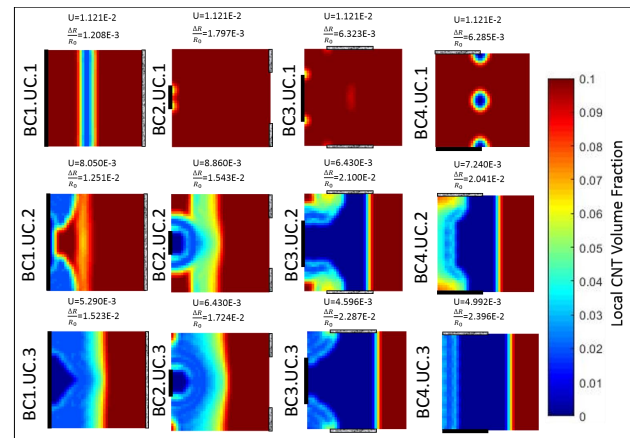


Fig. 15 Comparing topologies without a volume fraction constraint. Black and grey bars are used to mark electrode locations on the cross-sections. Labels associate the topology with its associated Pareto point in Figure 14.

sistive volume fractions are only used on the left half of the design.

5.3 Comparing Results Across All Constraint Values

A final summary of the results is presented in Figure 16. The boundary conditions are sorted by line and marker color, and the volume fractions constraints are sorted by marker shape, with the two percent volume fraction constraint solutions being marked by circles and the unconstrained solutions marked by squares.

As could be expected, the unconstrained solutions dominate their constrained counterparts. However, and examination of the total amount of CNTs used in the unconstrained designs shows that not all of the material is used in designs where sensing performance is valued. Table 3 shows objective values against total vol-

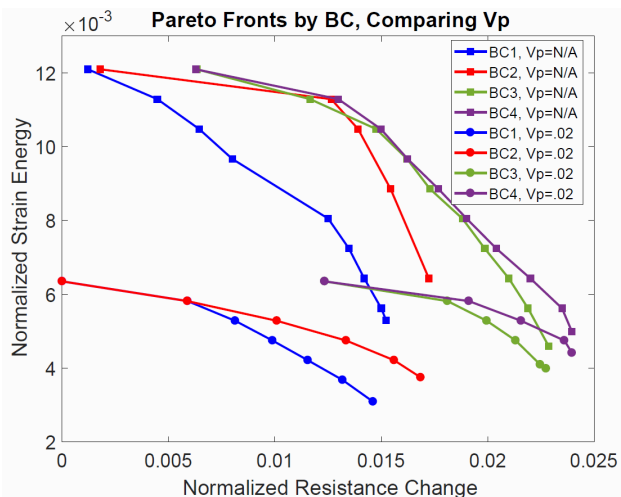


Fig. 16 Comparing Pareto Fronts across different volume fractions and boundary conditions

Table 3 Total volume fraction vs optimized resistance change and strain energy. Best performers highlighted.

ID	Global VF	Norm. U	Norm. $\frac{\Delta R}{R_0}$
1.UC.1	9.38%	1.210E-2	1.208E-3
1.UC.2	7.96%	8.050E-3	1.251E-2
1.UC.3	5.76%	5.290E-3	1.523E-2
2.UC.1	9.96%	1.210E-2	1.797E-3
2.UC.2	7.58%	8.860E-3	1.543E-2
2.UC.3	6.02%	6.430E-3	1.724E-2
3.UC.1	9.95%	1.210E-2	6.323E-3
3.UC.2	4.50%	6.430E-3	2.100E-2
3.UC.3	3.42%	4.596E-3	2.287E-2
4.UC.1	9.53%	1.210E-2	6.285E-3
4.UC.2	4.81%	7.240E-3	2.041E-2
4.UC.3	3.43%	4.992E-3	2.396E-2

ume fraction used for the labeled unconstrained optimal topologies. When large strain energies are required by the constraint, the optimal solution uses nearly all of the available material for the highest attainable strain energy. When strain energy constraint is relaxed and resistance change increases, the optimal solution uses less CNT, down to less than 4 percent for the highest resistance change values.

6 Conclusions

An optimization algorithm was developed to solve multiobjective topology optimization problems with multiple minima. The method implements micromechanics to obtain local effective properties, which are used within analytic beam bending and electrostatic finite element solutions to obtain measure of cross-sectional stiffness and strain sensing, respectively. Analytic gra-

dients are used to obtain sensitivities of the objectives with respect to the design variables.

A Pareto-based restart method was introduced to efficiently obtain improved Pareto Fronts. The method uses a two-stage optimization procedure in which Pareto points from a simplified problem (in the form of a coarse mesh representation of the design space) are used as starting conditions for the fine scale problem. In the example shown the Pareto-Based Restart method was computationally less expensive than a multi-start method with random initial topologies, and also resulted in a significantly better defined Pareto Front.

Four different boundary conditions and two different global volume fraction constraints were compared. It was found that relaxing the global volume fraction constraint directly improved strain energy results. The optimal topology without a global volume fraction constraint has over 90% more strain energy than the optimal topology with a two percent volume fraction constraint. In the case of the constant curvature beam strain energy is maximized by placing high CNT volume fractions as far from the neutral axis as possible.

Relaxing the global CNT volume fraction constraint also improves resistance change. However, the best sensing topologies did not use all available material, preferring between three and four percent CNT. For a given boundary condition, resistance change is maximized via shifting the neutral axis, creating piezoresistive asymmetry across the strain field, and developing a conductive path between the boundary electrodes. Placing the electrodes such that the conductive path does not have to cross the neutral axis leads to topologies that can perform well in both stiffness and sensing.

This study shows that the electrode boundary condition plays an important role in the sensing performance. In the future it may be beneficial to not only design the CNT distribution, but the electrode location as well. Also, extending the mechanics presented here and their associated sensitivities to 2D and 3D structures, relaxation of randomly oriented and well dispersed assumptions, or inclusion of additional nanomaterial additives are all interesting avenues of further investigation.

7 Acknowledgments

The authors would like to acknowledge the support of the Air Force Research Laboratory under agreement number FA8650-09-2-3938. This material was cleared under case number 88ABW-2018-3771.

References

- Alamusi, Hu, N., Fukunaga, H., Atobe, S., Liu, Y., Li, J.: Piezoresistive Strain Sensors Made from Carbon Nanotubes Based Polymer Nanocomposites. *Sensors* **11**(12), 10691–10723 (2011)
- Alamusi, Hu, N., Fukunaga, H., Atobe, S., Liu, Y., Li, J.: Piezoresistive Strain Sensors Made from Carbon Nanotubes Based Polymer Nanocomposites. *Sensors* **11**(12), 10691–10723 (2011). DOI 10.3390/s111110691. URL <http://www.mdpi.com/1424-8220/11/11/10691/>
- Bauhofer, W., Kovacs, J.Z.: A review and analysis of electrical percolation in carbon nanotube polymer composites. *Composites Science and Technology* **69**(10), 1486–1498 (2009)
- Bendsoe, M.P., Sigmund, O.: *Topology optimization by distribution of isotropic material*, pp. 1–69. Springer Berlin Heidelberg, Berlin, Heidelberg (2004)
- Chaurasia, A.K., Seidel, G.D.: Computational micromechanics analysis of electron-hopping-induced conductive paths and associated macroscale piezoresistive response in carbon nanotube-polymer nanocomposites. *Journal of Intelligent Material Systems and Structures* **25**(17), 2141–2164 (2014). DOI 10.1177/1045389X13517314. URL <http://journals.sagepub.com/doi/10.1177/1045389X13517314>
- Chaurasia, A.K., Sengazer, E.C., Talamadupula, K.K., Povolny, S., Seidel, G.D.: Experimental characterization and computational modeling of deformation and damage sensing through the piezoresistive response of nanocomposite bonded surrogate energetic materials. *Journal of Multifunctional Composites* **2**(4) (2014)
- Deaton, J.D., Grandhi, R.V.: A survey of structural and multidisciplinary continuum topology optimization: post 2000. *Structural and Multidisciplinary Optimization* **49**(1), 1–38 (2014)
- Ehrgott, M., Gandibleux, X.: A survey and annotated bibliography of multiobjective combinatorial optimization. *OR-Spektrum* **22**(4), 425–460 (2000)
- Eshelby, J.D.: The Determination of the Elastic Field of an Ellipsoidal Inclusion, and Related Problems. *Proceedings of the Royal Society of London A: Mathematical, Physical and Engineering Sciences* **241**(1226), 376–396 (1957)
- Gang Yin, N.H.: A carbon nanotube/polymer strain sensor with linear and anti-symmetric piezoresistivity. *Journal of Composite Materials* **45**(12), 1315–1323 (2011)
- Giurgiutiu, V., Zagrai, A., Bao, J.J.: Piezoelectric wafer embedded active sensors for aging aircraft structural health monitoring. *Structural Health Monitoring* **1**(1), 41–61 (2002). URL <http://shm.sagepub.com/content/1/1/41.short>
- Glaessgen, E., Stargel, D.: The digital twin paradigm for future nasa and us air force vehicles. In: 53rd AIAA/ASME/ASCE/AHS/ASC Structures, Structural Dynamics and Materials Conference 20th AIAA/ASME/AHS Adaptive Structures Conference 14th AIAA, p. 1818 (2012)
- Hammerand, D.C., Seidel, G.D., Lagoudas, D.C.: Computational Micromechanics of Clustering and Interphase Effects in Carbon Nanotube Composites. *Mechanics of Advanced Materials and Structures* **14**(4), 277–294 (2007). DOI 10.1080/15376490600817370. URL <http://www.tandfonline.com/doi/abs/10.1080/15376490600817370>
- Hwang, C.L., Masud, A.S.M.: Methods for multiple objective decision making. In: *Multiple Objective Decision Making Methods and Applications*, pp. 21–283. Springer (1979)
- Ivanova, O., Williams, C., Campbell, T.: Additive manufacturing (am) and nanotechnology: promises and challenges. *Rapid Prototyping Journal* **19**(5), 353–364 (2013)
- Keulemans, G., Ceyssens, F., De Volder, M., Seo, J.W., Puers, R.: Fabrication and characterisation of carbon nanotube composites for strain sensor applications. In: *Proceedings of the 21st Micromechanics and Micro systems Europe Workshop*, vol. 21, pp. 231–234 (2010)
- Kim, Y.Y., Kim, T.S.: Topology optimization of beam cross sections. *International Journal of Solids and Structures* **37**(3), 477–493 (2000)
- de Kruijf, N., Zhou, S., Li, Q., Mai, Y.W.: Topological design of structures and composite materials with multi-objectives. *International Journal of Solids and Structures* **44**(22-23), 7092–7109 (2007)
- Maute, K., Tkachuk, A., Wu, J., Jerry Qi, H., Ding, Z., Dunn, M.L.: Level set topology optimization of printed active composites. *Journal of Mechanical Design* **137**(11), 111402–111402–13 (2015). DOI 10.1115/1.4030994. URL <http://dx.doi.org/10.1115/1.4030994>
- Mavrotas, G.: Effective implementation of the ϵ -constraint method in multi-objective mathematical programming problems. *Applied mathematics and computation* **213**(2), 455–465 (2009)
- Mori, T., Tanaka, K.: Average stress in matrix and average elastic energy of materials with misfitting inclusions. *Acta metallurgica* **21**(5), 571–574 (1973)
- Obitayo, W., Liu, T.: A review: Carbon nanotube-based piezoresistive strain sensors. *Journal of Sensors* **2012**, 1–15 (2012). URL <http://www.hindawi.com/journals/js/2012/652438/>
- Oskouyi, A., Sundararaj, U., Mertiny, P.: Tunneling Conductivity and Piezoresistivity of Composites Containing Randomly Dispersed Conductive Nano-Platelets. *Materials* **7**(4), 2501–2521 (2014)
- Oskouyi, A., Sundararaj, U., Mertiny, P.: Tunneling Conductivity and Piezoresistivity of Composites Containing Randomly Dispersed Conductive Nano-Platelets. *Materials* **7**(12), 2501–2521 (2014). DOI 10.3390/ma7042501. URL <http://www.mdpi.com/1996-1944/7/4/2501>
- Postiglione, G., Natale, G., Griffini, G., Levi, M., Turri, S.: Conductive 3d microstructures by direct 3d printing of polymer/carbon nanotube nanocomposites via liquid deposition modeling. *Composites Part A: Applied Science and Manufacturing* **76**, 110–114 (2015)
- Reuss, A.: Berechnung der fliegrenze von mischkristallen auf grund der plastizitätsbedingung fr einkristalle. *ZAMM - Journal of Applied Mathematics and Mechanics / Zeitschrift fr Angewandte Mathematik und Mechanik* **9**(1), 49–58 (1929)
- Reuss, A.: Berechnung der fließgrenze von mischkristallen auf grund der plastizitätsbedingung für einkristalle. *ZAMM-Journal of Applied Mathematics and Mechanics/Zeitschrift für Angewandte Mathematik und Mechanik* **9**(1), 49–58 (1929)
- Roberts, S.C., Aglietti, G.S.: Satellite multi-functional power structure: Feasibility and mass savings. *Proceedings of the IMechE* **222**(1), 41–51 (2008). URL <http://journals.sagepub.com/doi/abs/10.1243/09544100JAERO255>
- Rubio, W.M., Silva, E.C.N., Nishiwaki, S.: Piezoresistive sensor design using topology optimization. *Structural and Multidisciplinary Optimization* **36**(6), 571–583 (2008)

30. Sairajan, K.K., Aglietti, G.S., Mani, K.M.: A review of multifunctional structure technology for aerospace applications. *Acta Astronautica* **120**, 30–42 (2016)
31. Sandler, J., Kirk, J., Kinloch, I., Shaffer, M., Windle, A.: Ultra-low electrical percolation threshold in carbon-nanotube-epoxy composites. *Polymer* **44**(19), 5893–5899 (2003)
32. Sardan, O., Eichhorn, V., Petersen, D.H., Fatikow, S., Sigmund, O., Bggild, P.: Rapid prototyping of nanotube-based devices using topology-optimized microgrippers. *Nanotechnology* **19**(49), 495503 (2008)
33. Schueler, R., Petermann, J., Schulte, K., Wentzel, H.P.: Agglomeration and electrical percolation behavior of carbon black dispersed in epoxy resin. *Journal of Applied Polymer Science* **63**(13), 1741–1746 (1997)
34. Seidel, G.D., Lagoudas, D.C.: Micromechanical analysis of the effective elastic properties of carbon nanotube reinforced composites. *Mechanics of Materials* **38**(8), 884 – 907 (2006). DOI <https://doi.org/10.1016/j.mechmat.2005.06.029>. URL <http://www.sciencedirect.com/science/article/pii/S0167663605001699>. *Advances in Disordered Materials*
35. Sigmund, O., Petersson, J.: Numerical instabilities in topology optimization: a survey on procedures dealing with checkerboards, mesh-dependencies and local minima. *Structural optimization* **16**(1), 68–75 (1998)
36. Sigmund, O., Torquato, S.: Design of materials with extreme thermal expansion using a three-phase topology optimization method. *Journal of the Mechanics and Physics of Solids* **45**(6), 1037 – 1067 (1997)
37. Stanford, B., Ifju, P.: Aeroelastic topology optimization of membrane structures for micro air vehicles. *Structural and Multidisciplinary Optimization* **38**(3), 301–316 (2009)
38. Swan, C.C., Kosaka, I.: Voigt-reuss topology optimization for structures with linear elastic material behaviours. *International Journal for Numerical Methods in Engineering* **40**(16), 3033–3057 (1997)
39. Talreja, R., Singh, C.V.: *Damage and Failure of Composite Materials*, 1 edition edn. Cambridge University Press, Cambridge, New York (2012)
40. Voigt, W.: Theoretische Studien ber die Elasticittsverhlt-nisse der Krystalle II. *Abhandlungen der Kniglichen Gesellschaft der Wissenschaften in Gttingen* (1887)
41. Xiao, J., Li, Y., Fan, W.: A laminate theory of piezoresistance for composite laminates. *Composites science and technology* **59**(9), 1369–1373 (1999)
42. Zegard, T., Paulino, G.H.: Bridging topology optimization and additive manufacturing. *Structural and Multidisciplinary Optimization* **53**(1), 175–192 (2016)
43. Zhu, R., Pan, E., Roy, A.: Molecular dynamics study of the stressstrain behavior of carbon-nanotube reinforced Epon 862 composites. *Materials Science and Engineering: A* **447**(1-2), 51–57 (2007)